chimpanzee carried 11 differences, the fact that the extent of variation among the clones remains unknown makes any statement about their taxonomic affiliation tenuous. Further complicating these analyses is the fact that nuclear insertions may have inserted before the divergence of primate species and may thus be similar or identical in different species, even though their organellar mtDNAs have diverged (*5*–*7*).

To determine more reliably the species used to produce these OPVs, a 141-bp segment (with primers) of the nuclear 28*S* rDNA gene was amplified. All samples except the cell culture control and one OPV sample (W Ch 25) yielded amplification products. These products were cloned, and sequences of 10 clones from each product contained only one DNA sequence per product. In order to compare these DNA sequences to the relevant species, the same DNA segment was determined from five old-world monkeys (*Macaca fascicularis*, *Macaca nemestrina*, *Colobus guereza*, *Chlorocebus aethiops*, *Nasalis larvatus*), one central chimpanzee (*Pan troglodytes troglodytes*), one eastern chimpanze (*P. t. schweinfurthii*), a bonobo (*P. paniscus*), and a human (*8*). The CHAT batch grown in human cells, as well as the Sabin I vaccine, carried a sequence identical to human (Table 1). This sequence differs at one position from bonobo and at two positions from the chimpanzees. All other OPV batches, including CHAT pool 13, yielded one and the same sequence. This sequence is seven nucleotides shorter than the chimpanzee and human sequences and differs at a minimum of 10 positions from the latter species. However, the sequence is identical to *M. fascicularis* and *M. nemestrina* as well as the macaque and mangabey controls obtained by the Wistar Institute from the CDC and included in the original set of 14 unidentified samples.

Because it has been claimed that chimpanzee tissues were cultured at the Wistar Institute at the time of the production of CHAT pool 13 (*2*), it may be argued that the monkey cell cultures used to produce the OPV could have been deliberately or accidentally combined with chimpanzee cells. Such an occurrence would mean that DNA from two species (monkey and chimpanzee) would be present in the OPV samples, with any chimpanzee DNA perhaps being in relatively low abundance. To investigate this possibility, we designed a set of primers that were expected to amplify a 128-bp piece (with primers) of the internal transcribed spacer 1 in the nuclear ribosomal gene cluster of chimpanzees and bonobos, but not from other species. As expected, these primers amplified the chimpanzee and bonobo gene fragments, but failed to amplify the correct fragment from 100 ng of DNA from *Chlorocebus aethiops*, *Nasalis larvatus*, *Colobus guereza*, *Macaca fascicularis*, or humans. By using a dilution series of chimpanzee DNA, it was shown that the primers yielded a visible product from as few as 10 to 50 template DNA copies. Finally, it was tested whether low amounts of chimpanzee DNA could be masked by the presence of monkey DNA. To this end, 50 ng of *M. fascicularis* DNA was mixed with 200, 100, 50, and 5 pg of chimpanzee DNA. In all cases, a strong amplification product of the correct size could be visualized on an agarose gel (*9*). Thus, even in the presence up to a 10,000-fold excess of macaque DNA, chimpanzee DNA was detected by this assay. When these primers were used to amplify from 5 μl of the OPV samples, no amplification products of the correct size could be detected. Assuming that the ape genome contains on the order of 1000 ribosomal genes, this result means that any chimpanzee DNA present in the vaccines must represent less than about one chimpanzee cell per 100 μl of vaccine, or <0.01% of the total DNA present in those samples whose total DNA concentration would allow the detection of such a small DNA component (e.g., CHAT pool 13 and CDC CHAT pool 13).

In conclusion, most of the DNA present in the OPV batches we analyzed is derived from old-world monkeys and not from chimpanzees or bonobos, as previously stated (*10*). It is unlikely that undetected chimpanzee DNA is present, based on the finding that most of the OPV samples, including pool 13 from the Wistar Institute, contain amounts of amplifiable DNA that should make amplifications reproducible. Furthermore, substantial contamination of the tissue cultures used for vaccine production by chimpanzee cells is unlikely, since chimpanzee DNA would have been detected if it constituted >0.01% of the total DNA in the vaccines. Obviously, the samples tested in this study represent only one of maybe four vaccine batches produced by the Wistar Institute and used in the Congo (*11*). However, the results at present give no support for the hypothesis that chimpanzee cells were used to produce the OPV administered in the Congo in 1958 and 1959.

References and Notes

1. T. Curtis, *Rolling Stone* (no. 626) (1992), p. 54.
2. E. Hooper, *The River: A Journey to the Source of HIV and AIDS* (Little Brown, New York, 1999).
3. Amplifications were conducted on material directly from all samples. Hot-start PCR was conducted using Amplitaq Gold (Perkin-Elmer, Germany) as per manufacturer's instructions. Cycling parameters were as follows: 94°C for an initial 4 min, followed by 92°C for 15 s, 57°C for 1 min, and 72°C for 1 min. This was cycled 45 times. PCR products were cloned into TA cloning vectors (Invitrogen, Netherlands). Colonies were sequenced as described [C. Kilger, M. Krings, H. Poinar, S. Pääbo, *BioTechniques* **22**, 412 (1997)]. Primers used were: MT12Sa', 5'-CTGGGATTAGATACCCACTAT-3'; MT12So, 5'-GTCGATTATAGGACAGGTTCCTCTA-3'; NU28SL, 5'-GGTCGTCCGACCTGGGTATA-3'; NU28SR, 5'-TCTAATCATTCGCTTTACCGGAT-3'; NUITS3F, 5'-CTCTCCGGAGTCCGGTCCCGTTTTTG-3'; NUITS3R, 5'-GGCGAGGGCGCTCCCGACAACA-3'.
4. P. A. Morin, K. E. Chambers, C. Boesch, L. Vigilant, *Mol. Ecol.*, in press.
5. A. D. Greenwood, S. Pääbo, *Mol. Ecol.* **8**, 133 (1998).
6. R. Collura, C. Stewart, *Nature* **378**, 485 (1995).
7. A. C. van der Kuyl, C. L. Kuiken, J. T. Dekker, W. R. Perizonius, J. Goudsmit, *J. Mol. Evol.* **40**, 173 (1995).
8. Supplementary figure is available at www.sciencemag.org/cgi/content/full/292/5517/743/DC1.
9. H. Poinar, M. Kuch, S. Pääbo, data not shown.
10. S. A. Plotkin, B. J. Cohen, H. Koprowski, *Virology* **15**, 473 (1961).
11. S. A. Plotkin, *Clin. Infect. Dis.* **32**, 1068 (2001).

12. We thank C. Basilico, C. Buck, D. Ewert, S. Kwok, A. C. van der Kuyl, D. Poinar, L. Vigilant, S. Wain-Hobson, and H. Zischler for help and sharing of unpublished information. We thank the Max Planck Society and the Deutsche Forschungsgemeinschaft for financial support.

20 December 2000; accepted 28 February 2001

Virus Maturation Involving Large Subunit Rotations and Local Refolding

J. F. Conway,[1,2] W. R. Wikoff,[3] N. Cheng,[1] R. L. Duda,[4] R. W. Hendrix,[4] J. E. Johnson,[3] A. C. Steven[1]*

Large-scale conformational changes transform viral precursors into infectious virions. The structure of bacteriophage HK97 capsid, Head-II, was recently solved by crystallography, revealing a catenated cross-linked topology. We have visualized its precursor, Prohead-II, by cryoelectron microscopy and modeled the conformational change by appropriately adapting Head-II. Rigid-body rotations (~40 degrees) cause switching to an entirely different set of interactions; in addition, two motifs undergo refolding. These changes stabilize the capsid by increasing the surface area buried at interfaces and bringing the cross-link–forming residues, initially ~40 angstroms apart, close together. The inner surface of Prohead-II is negatively charged, suggesting that the transition is triggered electrostatically by DNA packaging.

A recurring theme in virus assembly is the initial formation of a precursor particle or procapsid that subsequently transforms into the mature capsid. In general, procapsids and capsids differ markedly in structure. Procapsids were first observed among the double-stranded DNA (dsDNA) bacteriophages (*1*, *2*), but have now also been observed for

herpesviruses (*3*), retroviruses (*4*), dsRNA phages (*5*), and an insect virus (*6*). In the course of normal infections, procapsids mature shortly after they are assembled and do not accumulate unless maturation is blocked—for example, by inhibiting the viral protease or the packaging of nucleic acid.

The consequences of maturation vary from system to system, although certain features are common to most procapsids; in particular, their hexamers show large departures from sixfold symmetry, and the procapsid is round, in contrast to the polyhedral mature capsid. Possible changes upon maturation may include the protein composition, with scaffolding proteins being expelled and accessory proteins binding to newly exposed sites; translocation of epitopes between the inner and outer surfaces (*7*, *8*); alteration of secondary structure (*9*, *10*); and autocatalytic formation of covalent cross-links between neighboring subunits (*11*). However, these changes all reflect the primary underlying mechanism—a major conformational change of the capsid protein, preceded in many cases by the action of a viral protease.

These transitions are irreversible and their energetic basis lies in exothermic switching from one local minimum of conformational free energy to another, lower-energy, state (*12*). The concomitant structural changes are known to be large, but their basis has not been determined in any system; in principle, they may involve rigid-body motions of subunits, order-disorder transitions, or refolding (*13*). HK97 affords an advantageous system to study this phenomenon. The assembly pathway of its single 385-residue capsid protein is well characterized (*14*, *15*). Maturation begins with proteolysis of the 102-residue Δ-domains on the earliest precursor Prohead-I, producing Prohead-II, followed by expansion—the major structural change—and cross-linking.

At 12 Å resolution, the distinctive shear of Prohead-II hexamers is less conspicuous than at 25 Å resolution (*16*) (compare Fig. 1, B and C), on account of the abundant detail that is now overlaid. Despite the complexity of the map, matching features—such as the triplets of small knobs clustered around the threefold axes on the outer surface—are found on all subunits. The inner surface, whose main feature is the cavities underlying each capsomer, is resolved into a complex matrix of ridges and crevices (Fig. 1D). There are small holes at the quasi-threefold positions around the pentamers, as well as near-tangential channels of about the same diameter (Fig. 1D). Because the Δ-domains and the protease are not present in Prohead-II (*16*), the small dimensions of the observed channels—which represent the most likely exit routes—imply that they are reduced to fragments before release (*17*).

The most conservative mode of conformational change involves rigid-body displacements of the subunits, which have a core—the A and P domains—and two extended motifs, the E-loop and the N-arm (Fig. 2A). To test this hypothesis, we shifted the subunits from their known positions in Head-II (*15*) to fit the Prohead-II density map. Initially, this operation was performed interactively, with molecular graphics (*18*) and visual criteria. This fit was then refined automatically, with each of the seven quasi-equivalent subunits treated separately. The resulting fit was generally excellent, but discrepancies were encountered involving the E-loop and the N-arm, which are the motifs that exhibit the greatest variation among the seven quasi-equivalent subunits of Head-II (*15*). Because the discrepancies were observed consistently for all seven subunits, we concluded that these peptides undergo refolding.

One discrepancy involved the knobs around the threefold axes that accommodate the E-loops, and was partly resolved by swiveling them by ~15° relative to the core domains (Fig. 2A). These movements are similar to, but larger than, E-loop variations between different Head-II subunits. However, the E-loop tips still protruded from the knobs to an extent that was significant in view of the absence of similar excursions elsewhere (Fig. 2D). We infer that either they are folded differently than in Head-II or are disordered. Taking into account both rotations, the E-loops in Prohead-II extend radially outward, whereas in Head-II, they are

[1]Laboratory of Structural Biology Research, National Institute of Arthritis, Musculoskeletal and Skin Diseases, Bethesda, MD 20892, USA. [2]Institut de Biologie Structurale–J.-P. Ebel, 41 rue Jules Horowitz, 38027 Grenoble, France. [3]Department of Molecular Biology, Scripps Research Institute, La Jolla, CA 92037, USA. [4]Department of Biological Sciences, University of Pittsburgh, Pittsburgh, PA 15260, USA.

*To whom correspondence should be addressed at Building 6, Room B2-34, 6 Center Drive MSC 2717, NIH, Bethesda, MD 20892–2717, USA. E-mail: alasdair_steven@nih.gov

Table 1. Subunit movements in the Prohead-II to Head-II transition.

Subunit	Distance (Å)*	Rotation angle (°)†	Cross-link distance Prohead-II (Å)‡	Cross-link distance Head-II (Å)‡
A	53	24	32	9
B	45	39	31	7
C	45	36	34	8
D	45	20	39	9
E	42	36	37	8
F	51	37	39	8
G	58	22	33	9

*Distance between the subunit center of mass of Prohead-II and Head-II. †The rotation angle between the Prohead-II and Head-II subunit. ‡Distance between Cα atoms of Lys^{169} in the indicated subunit and Asn^{356} in the subunit that is cross-linked (Head-II) or will be cross-linked (Prohead-II).

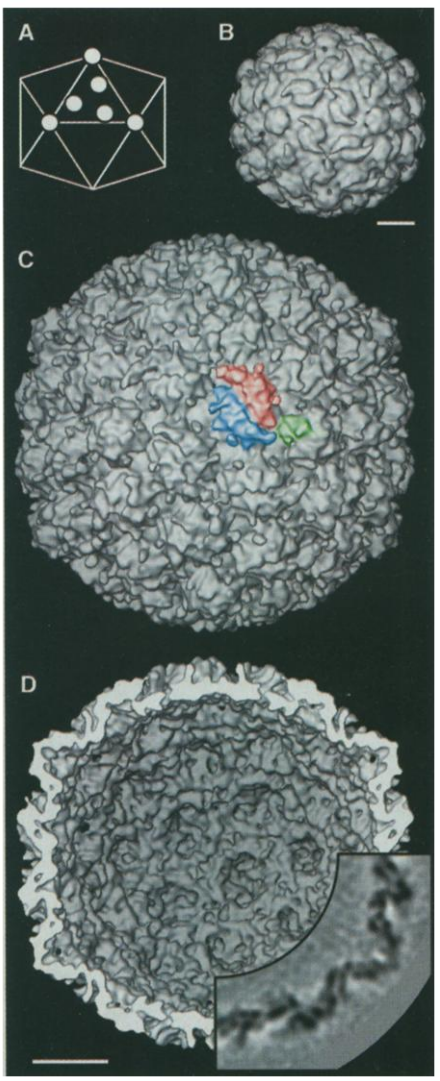

Fig. 1. HK97 Prohead-II at 12 Å resolution, as viewed along a twofold axis (*33*). (**A**) Diagram showing placement of capsomers (hexamers and pentamers) on an icosahedral surface lattice, triangulation number $T = 7$ *laevo*. (**B**) Prohead-II at 25 Å resolution (*16*). (**C**) Exterior view of Prohead-II, with one hexamer colored in red and blue, corresponding to its two trimers related by a 30 Å "shear" dislocation, and the pentamer subunit in green to complete the asymmetric unit. The contour level corresponds to 100% of expected mass. (**D**) Interior view of Prohead-II. The section plane (bottom right quadrant) illustrates the low noise level of the map. Bars, 100 Å.

tangential to the capsid surface (compare Fig. 2, B and C). In this way, the premature formation of cross-links is prevented: Lys^{169} is in the E-loop knob of Prohead-II, 30 to 40 Å from the Asn^{356} of a neighboring subunit with which it will cross-link in Head-II (Table 1). This shift also explains why Lys^{166}, which is also in the E-loop, is susceptible to trypsin in Prohead-II (Fig. 2A) but not in Head-II (*14*).

The second discrepancy was a steric clash involving the N-arms. We were unable to find a unique alternative conformation for them, and so omitted the first 23 residues from the final model. Nevertheless, assuming that the protease acts from inside the capsid, their NH_2-termini, being distal to the cleavage site, should be on the inner surface.

The pseudo-atomic model of Prohead-II is compared with Head-II in Fig. 2B. The hexamer is a dimer of trimers, with subunits B-C-D and E-F-A, respectively. The displacements vary among the quasi-equivalent subunits but are typically large, with rotations of ~40° and radial translations of ~50 Å (Table 1 and Fig. 3A). Although Prohead-II changes radically in size, shape, and surface relief as it expands, the structural core of its subunits (the A and P domains) is conserved. These core elements undergo "tumbling" displacements, accompanied by refolding of the E-loop and the N-arm. The latter effect is reminiscent of the different configurations of the terminal peptides of SV40 capsid protein linking its capsomers (*19*), and the poliovirus cell entry transition in which a terminal peptide, initially inside the virion, is flipped outside (*20*).

The mature capsid must be stable enough to resist the pressure imposed by densely packaged DNA and other challenges (*1*). Our model of the transition indicates how stabilization is accomplished. Although the shell becomes thinner upon maturation, the surface area buried at intermolecular interfaces increases markedly (Table 2). By this measure, intersubunit interactions within a capsomer (hexamer or pentamer) increase by ~35%, and interactions between capsomers by ~64%. Further stabilization is conferred by the cross-links formed between pairs of residues, initially up to 40 Å apart in Prohead-II

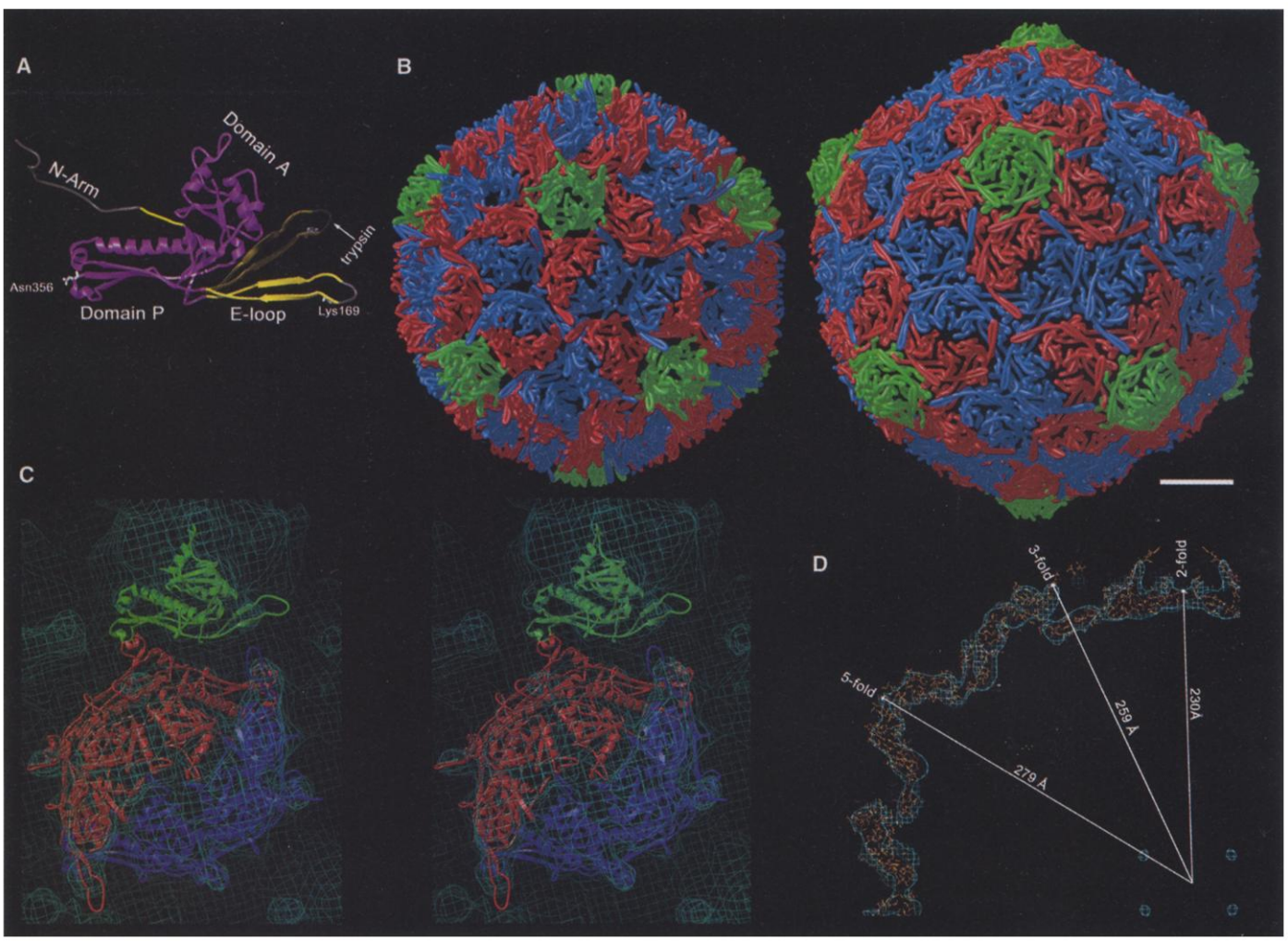

Fig. 2. Pseudo-atomic model of Prohead-II. (**A**) The Head-II subunit has two compact domains, A and P (magenta), with two flexible extensions, the N-arm and E-loop (yellow and gray) (*15*). The gray portion of the N-arm was omitted from the Prohead-II model. Both conformations of the hinged E-loop are shown: as in Prohead-II (semitransparent, with the trypsin-sensitive site marked) and as in Head-II (yellow). Asn^{356} and Lys^{169} engage in intermolecular cross-links in Head-II. (**B**) Prohead-II (left) and Head-II (right). Each subunit is represented as a tube, constructed from a "smoothed" Cα backbone; pentamers are green and hexamers consist of two skewed trimers, blue and red, respectively. During expansion, the hexamer skew dislocation is eliminated (*16*, *28*); the hexamers become almost perfectly sixfold symmetric; and the angle between hexamer and pentamer increases, producing a flatter surface. (**C**) Stereo view of the asymmetric unit of Prohead-II, consisting of a pentamer subunit and a hexamer, colored as in (B); the pseudo-atomic model is enclosed within the density map. The E-loop forms a well-defined knob for each subunit; the angle between the loop and domain P was adjusted at the "hinge" [yellow/magenta interface in (A)]. The N-arm was adjusted as a rigid-body, hinged about Arg^{130}. (**D**) Cross section of the Prohead-II model (yellow) and map (cyan). The maximum radius is 279 Å at the fivefold axes, compared with 330 Å in Head-II. As packed in Prohead-II, the pentamers and hexamers protrude, revealing a corrugated outer surface.

but brought close together in Head-II.

It appears likely that similar mechanisms effect maturation for other viruses; for example, subunit rotations would explain the translocation of T4 epitopes between its inner and outer surfaces (*7*, *8*). The lambda (*21*) and P22 (*22*) procapsids exhibit similar skewing of their hexamers and structural changes upon maturation, despite P22 having a quite different topography from HK97.

More generally, the basic mechanism underlying HK97 capsid maturation—domain rotations—resembles similar phenomena encountered in substrate binding by some enzymes [e.g., (*23*)] and in the reaction cycles of motor proteins (*24*) and chaperones (*25*), although the concomitant refolding of the E-loop and the N-arm appears to represent a further elaboration. There is, however, the significant distinction that capsid maturations are irreversible, not cyclic, events and their energy source is transduction of conformational free energy, not nucleotide hydrolysis.

The principle underlying protein self-assembly is the existence, on opposite sides of the same molecule, of surface patches with a mutual binding affinity. For polymerization into a closed shell, there must be at least two such pairs of complementary surfaces per subunit. For the nonequivalent 120-subunit capsids of dsRNA viruses (*26*), there should be four such pairs. Remarkably, this number is even higher for HK97. Proliferation occurs at two levels. First, the pronounced departures from equivalence in the sheared Prohead-II hexamer place subunits in different bonding environments. Second, during expansion, the subunits rotate, transferring the interactions to different surfaces, both for bonding within a capsomer and between capsomers (Fig. 3A).

Because the interactions engaged in Head-II should correspond to the lowest free-energy state, why are they not adopted at the outset? Capsid protein assembles into Prohead-I because association into pentamers and hexamers (*27*) produces building-blocks with the appropriate interaction surfaces exposed around their peripheries. We conjecture that interactions involving the Δ-domains contribute decisively to the overall bonding energy. In this way, they select the particular pair of complementary patches that is to be exposed around the capsomer and will mate when capsomers assemble into Prohead-I. Upon digestion of the Δ-domains, their contribution to the overall free energy is eliminated, and the expanded (Head) conformation becomes favored. However, the particle remains kinetically trapped as Prohead-II until some external stimulus such as acidification opens up a transitional pathway, and the expansion transformation propagates over its surface (*28*).

How is the transition triggered? Here, the surface charge of Prohead-II (Fig. 3, B to E) offers a clue. The subunit has a net negative charge, and most positive charges are buried at subunit interfaces. The inner surface of Prohead-II is negatively charged (Fig. 3C), with pockets lined by Asp^{136}, Glu^{219}, Glu^{220}, Asp^{337}, Glu^{364}, and Asp^{340}. In DNA packaging, the stiffness of incom-

Table 2. Buried surface areas per capsomer (Å^2).

	Prohead-II		Head-II‡	
	Pentamer	Hexamer	Pentamer	Hexamer
Intracapsomer*	15,665	17,694	21,720	23,277
Intercapsomer†	13,385	14,696	21,030	24,950

*Buried surface areas were calculated between adjacent pairs of subunits within a capsomer. †Buried surface areas were calculated between all subunits of a given capsomer and contacting subunits of neighboring capsomers. ‡By this measure, intra- and intercapsomer interactions contribute almost equally to capsid stabilization (*33*).

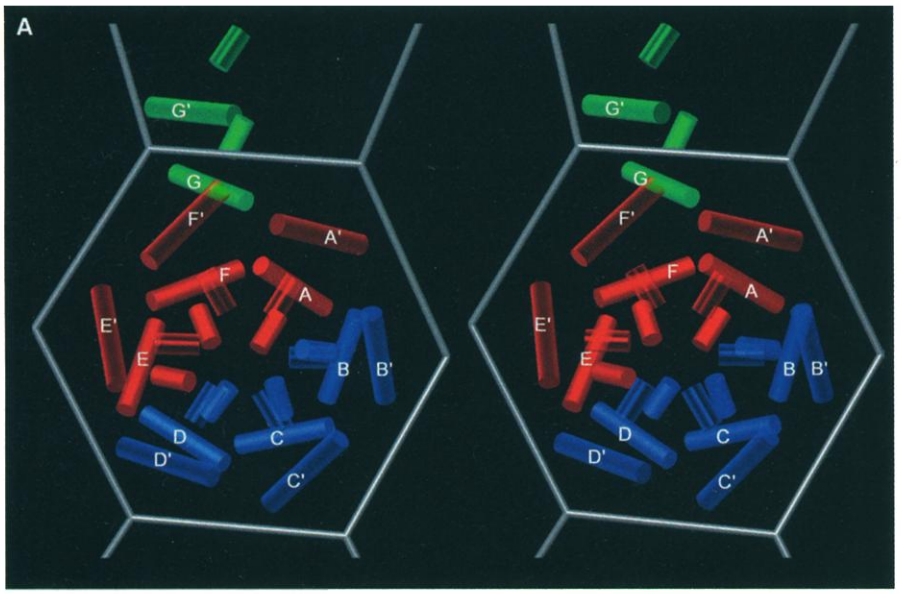

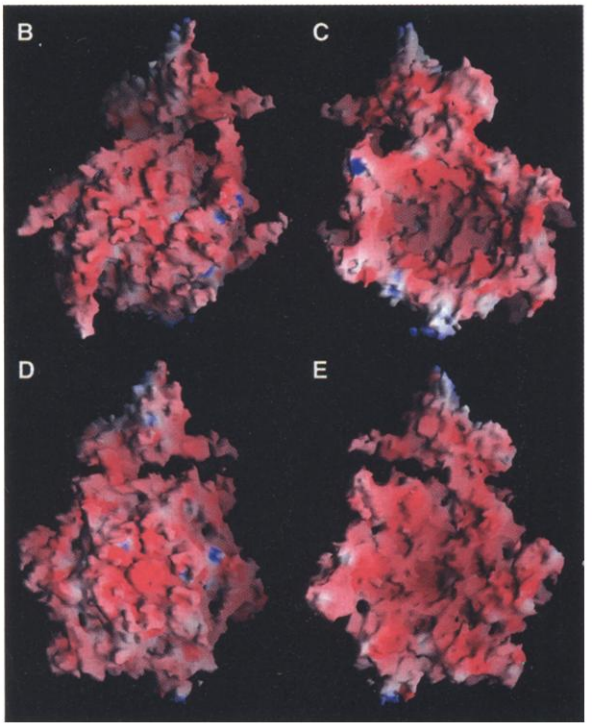

Fig. 3. (**A**) Stereo view showing a comparison of subunit positions and orientations in Prohead-II and Head-II. The capsid asymmetric unit is viewed from the exterior. Each subunit is represented by two helices (α3 and α6). Head-II is represented by semitransparent rods (labeled A′ to G′), and Prohead-II by solid rods (labeled A to G). Differences in subunit positions (Table 1) average ~50 Å, much of which represents outward radial movement, especially for pentamers. Part of a $T = 7$ lattice is superimposed in gray. (**B** to **E**) GRASP diagrams (*32*) showing the distribution of negative (red) and positive (blue) charge on the surfaces of Prohead-II (B and C) and Head-II (D and E). Shown in each case is an asymmetric unit consisting of a hexamer and one pentamer subunit. (B and D) Outside surfaces; (C and E) inner surfaces.

ing duplex DNA should coerce it to positions of high radius inside Prohead-II, where it will impose a repulsive force on the negatively charged inner surface. As packaging proceeds, this force should build up and—barring dominant counterion effects—eventually overcome the energetic barrier to expansion. The inner surface remains negatively charged after expansion (Fig. 3B), so that there is no net electrostatic attraction to the inner surface of the capsid to resist the exit of DNA during infection.

References and Notes

1. L. D. Simon, *Proc. Natl. Acad. Sci. U.S.A.* **69**, 907 (1972).
2. J. King, W. Chiu, in *Structural Biology of Viruses*, W. Chiu, R. M. Burnett, R. Garcea, Eds. (Oxford Univ. Press, New York, 1997), pp. 288–311.
3. B. L. Trus *et al.*, *J. Mol. Biol.* **263**, 447 (1996).
4. B. G. Turner, M. F. Summers, *J. Mol. Biol.* **285**, 1 (1999).
5. S. J. Butcher, T. Dokland, P. M. Ojala, D. H. Bamford, S. D. Fuller, *EMBO J.* **16**, 4477 (1997).
6. M. A. Canady, M. Tihova, T. N. Hanzlik, J. E. Johnson, M. Yeager, *J. Mol. Biol.* **299**, 573 (2000).
7. J. Kistler, U. Aebi, L. Onorato, B. ten Heggeler, M. K. Showe, *J. Mol. Biol.* **126**, 571 (1978).
8. A. C. Steven, A. C. Bauer, M. E. Bisher, F. A. Robey, L. W. Black, *J. Struct. Biol.* **106**, 221 (1991).
9. A. C. Steven, H. Greenstone, A. C. Bauer, R. W. Williams, *Biochemistry* **29**, 5556 (1990).
10. R. Tuma, P. E. Prevelige Jr., G. J. Thomas Jr., *Biochemistry* **35**, 4619 (1996).
11. R. L. Duda, *Cell* **94**, 55 (1998).
12. M. L. Galisteo, J. King, *Biophys. J.* **65**, 227 (1993).
13. M. S. Rossmann, J. W. Erickson, in *Virus Structure and Assembly*, S. Casjens, Ed. (Jones and Bartlett, Boston, 1985), pp. 29–74.
14. R. W. Hendrix, R. L. Duda, *Adv. Virus Res.* **50**, 235 (1998).
15. W. R. Wikoff *et al.*, *Science* **289**, 2129 (2000).
16. J. F. Conway, R. L. Duda, N. Cheng, R. W. Hendrix, A. C. Steven, *J. Mol. Biol.* **253**, 86 (1995).
17. R. L. Duda *et al.*, *J. Mol. Biol.* **247**, 618 (1995).
18. T. A. Jones, J. Y. Zou, S. W. Cowan, Kjeldgaard, *Acta Crystallogr. A* **47**, 110 (1991).
19. R. C. Liddington *et al.*, *Nature* **354**, 278 (1991).
20. C. E. Fricks, J. M. Hogle, *J. Virol.* **64**, 1934 (1990).
21. T. Dokland, H. Murialdo, *J. Mol. Biol.* **233**, 682 (1993).
22. Z. Zhang *et al.*, *J. Mol. Biol.* **297**, 615 (2000).
23. M. A. Schumacher *et al.*, *J. Mol. Biol.* **298**, 875 (2000).
24. J. D. Jontes, R. A. Milligan, *J. Cell. Biol.* **139**, 683 (1997).
25. Z. Xu, A. L. Horwich, P. B. Sigler, *Nature* **388**, 741 (1997).
26. R. H. Cheng *et al.*, *J. Mol. Biol.* **244**, 255 (1994).
27. Z. Xie, R. W. Hendrix, *J. Mol. Biol.* **253**, 74 (1995).
28. R. Lata *et al.*, *Cell* **100**, 253 (2000).
29. J. F. Conway, A. C. Steven, *J. Struct. Biol.* **128**, 106 (1999).
30. B. R. Brooks *et al. J. Comp. Chem.* **4**, 187 (1983).
31. A. Nicholls, K. Sharp, B. Honig *Proteins* **11**, 281 (1991).
32. M. K. Gilson, B. Honig *Proteins* **4**, 7 (1988).
33. P. D. Ross, L. W. Black, M. E. Bisher, A. C. Steven, *J. Mol. Biol.* **183**, 353 (1985).
34. Methods: Connectorless Prohead-II was produced and purified as described (*11*). Vitrified samples were imaged on a CM200-FEG (FEI, Mahwah, NJ) (*28*). Digitization was performed on a SCAI scanner (Z/I Imaging, Huntsville, AL). Image reconstruction, including contrast transfer correction, was done as described (*29*). Nine focal pairs were analyzed, yielding 2939 particles, of which 981 were included in the final map. This map was calculated to 12 Å, its resolution as assessed by Fourier Ring Correlation (cutoff, 2σ), as calculated between reprojections of two maps from half data sets. Moreover, the 420 small knobs (see above) were consistently visualized at this resolution. The subunit atomic model (*15*) was hand-fitted into the density map with the program O (*18*) and refined by X-PLOR 3.0 (Yale University, New Haven, CT). Structure factors and phases were calculated from the map and used as the experimental data set in refinement. Subunit positions were refined by rigid-body movements. The temperature factor for the model, optimized against the data, was determined to be 350 Å^2 and was applied throughout refinement. To avoid local minima, refinement was first performed to 25 Å resolution, then extended to 18 Å, and finally to 12 Å. At 25 Å, the subunit was treated as a single rigid body. At 18 Å, the E-loop was allowed to move as a separate rigid body, and Van der Waals repulsions were added to prevent steric clashes. The final model omitted residues 104 to 127 after an unsuccessful attempt to locate this peptide by calculating a difference map ($F_{map} - F_{model}$) in reciprocal space. The agreement between the pseudo-atomic model and the cryo-EM map was excellent (correlation 0.88, with the model limited to 12 Å resolution). Buried surface areas were calculated with CHARMM (*30*). The total area buried was calculated by identifying all subunit pairs within the icosahedral asymmetric unit (seven subunits) and between these subunits and all their contact neighbors, calculating the buried surface area for each pair, and summing. Residues 104 to 127 were omitted from Head-II, to equalize the number of residues for the comparison. Electrostatic calculations were performed with DELPHI (*31*) and displayed with GRASP (*32*).

35. We thank V. Reddy for buried surface calculations and D. Belnay and R. Wade for help with computing. Supported in part by NIH (R01 grants GM47795 to R.W.H. and AI40101 to J.E.J.) and by the NIH Targeted Antiviral Program (A.C.S.). The coordinates of the quasi-atomic model of Prohead-II have been deposited in the Protein Data Bank (1IF0).

6 December 2000; accepted 30 March 2001